Simulation of the SPARC Plasma Boundary with the UEDGE Code

S.B. Ballinger, A.Q. Kuang, M. V. Umansky[a], D. Brunner[b], J.M. Canik[c], M. Greenwald, J.D Lore[c], B. LaBombard, J.L. Terry, M. Wigram, and the SPARC team

MIT Plasma Science and Fusion Center, Cambridge, Massachusetts 02139, USA
[a]Lawrence Livermore National Laboratory, Livermore, California 94550, USA
[b]Commonwealth Fusion Systems, Cambridge, Massachusetts 02139, USA
[c]Oak Ridge National Laboratory, Oak Ridge, Tennessee 37831, USA
Contact: sballin@mit.edu

Abstract

In this work, the UEDGE edge transport code is used to examine conditions in the SPARC divertor and edge plasma for various levels of carbon impurity and power from the core (P_{SOL}). A double-null magnetic configuration is simulated assuming up-down symmetry in geometry and physics. The anomalous heat and particle transport coefficients are tuned to match empirical predictions for SPARC's midplane density profiles, target plate heat flux profiles, and inner/outer divertor power sharing. Convective transport is included on the low-field side, while on the high-field side the transport is modeled as purely diffusive. Hydrogen neutrals are modeled as a fluid with inertial effects, and a carbon impurity is included using the fixed-fraction model. We find that detachment induced by impurity seeding could significantly reduce the heat flux to the divertor surfaces in the SPARC tokamak. At $P_{SOL} = 28$ MW (the value predicted for SPARC's full-power H-mode scenario) cases with both divertor legs detached were obtained with a carbon impurity fraction between 0.3–1.4%, far below Z_{eff} limits for SPARC. When the plasma in the outer leg is detached, the peak heat flux density perpendicular to the target plate is below 1 MW/m^2, electron and ion temperatures are less than 1.5 eV, and momentum detachment is observed. However, the detachment state is found to be sensitive to the side-wall boundary conditions, the level of neutral pumping, and the target plate tilt. Finally, a broadly similar SOLPS simulation of SPARC is used to assess the appropriateness of the simpler impurity and neutral models used in UEDGE.

1. Introduction

The SPARC tokamak is currently being designed as a compact device with a magnetic field of 12 T targeting a fusion gain of $Q > 2$ [1]. The SPARC scenario of primary interest in this study is one for which 13 MW of external radiofrequency and ohmic heating is supplied, 20–28 MW of fusion alpha power and 113 MW of neutron power is produced, and 10–13 MW is radiated from the core. The amount of power crossing the separatrix and entering the scrape-off layer (SOL) is therefore taken to be $P_{SOL} = 28$ MW at "full power" for the purpose of simulation with UEDGE. This scenario is at the L-H threshold power, though a maximum of 25 MW of external heating power is available to provide some margin [2].

In the absence of significant dissipation in the SOL upstream, for example via radiation, the majority of the 28 MW of power into the SOL will be directed into the divertor legs, and the divertor surfaces may experience very high heat fluxes. Well-documented empirical scalings for the SOL heat flux width predict a narrow width between 0.18 and 0.4 mm, leading to an expected peak parallel heat flux greater than 10 GW/m^2 [2]. Full-power operation will be attempted with both single- and double-null equilibria. In a double-null equilibrium, power sharing between the inner and outer divertor is expected to have a ratio of 1:4 [3], resulting in a peak perpendicular heat flux of 25 MW/m^2 to the inner divertor target and 70 MW/m^2 to the outer target assuming a shallow incident field line angle and 50% radiation fraction (Figure 1).

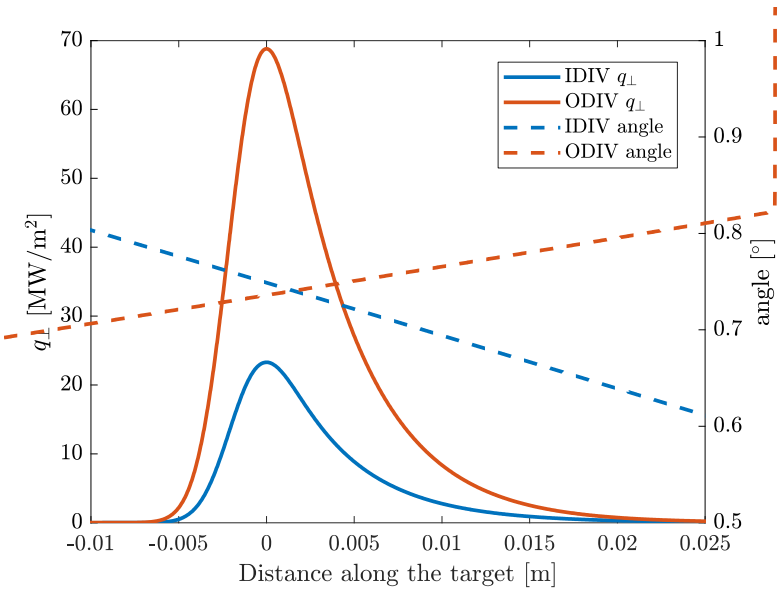

Figure 1: Prediction from empirical scalings of the perpendicular heat flux along the inner and outer divertor targets in a SPARC double-null configuration assuming a 50% radiation fraction.

Due to the high heat fluxes expected in the inertially cooled SPARC divertor, the tokamak is being designed with several heat flux mitigation measures: plasma pulses will be kept short (under 10 seconds), the incident field line angles in the divertor are designed to be under 1º (assuming toroidal symmetry—fish-scaling may be required to hide leading edges), and the strike-point on each target surface will be swept at a rate of ~1 Hz over 30-40 cm of poloidal arc length [2].

Beyond these baseline strategies, SPARC will also attempt to take advantage of divertor detachment, in which interactions of plasma with neutral hydrogen and impurity atoms result in volumetric energy losses, reducing plasma momentum, heat flux, and temperature at the divertor targets. Detachment is usually induced by puffing gases containing low-Z impurity atoms such as nitrogen or neon. In SPARC, if the plasma-facing components are made of a graphite-based material, sputtered carbon atoms could cause detachment.

A previous analysis estimated the impurity density as a fraction of the main ion density required to achieve detachment in tokamaks, including a SPARC-like device. The 0D model used empirical scalings for the heat flux width and L-H threshold power and a simple SOL radiation model, and found that for the divertor to detach in a SPARC-like device ($B_T = 12$ T, $R = 1.65$ m, $P_{SOL} = 48$ MW, and an upstream density of 6×10^{20} m^{-3}), the required impurity fraction is 11% using nitrogen, 4% using neon, and 3% using argon [4]. The latest SPARC design has $B_T = 12.2$ T, $R = 1.85$ m, $P_{SOL} = 30$ MW, and an upstream density of 10^{20} m^{-3} [1].

The estimates of the 0D model serve as a starting point for more advanced studies that take into account the SOL geometry and plasma profiles. In this work, we use the UEDGE code [5] to examine SOL plasma dynamics and detachment in SPARC in greater detail. UEDGE has recently been used to model advanced-divertor configurations, in particular the SOL of the ADX and ARC tokamak concepts [6,7]. Before this study, it was uncertain whether UEDGE would be able to model SPARC without issues due to the extremely small heat flux width and large average plasma pressure and parallel heat flux density [2,8].

2. Experimental Setup and Methods

UEDGE simulates ions, electrons, and neutrals as fluids in a 2D axisymmetric grid from the outer core of the plasma to the outer edge of the SOL. The model includes the Braginskii fluid equations, tabulated rates of radiation, ionization, recombination, and charge exchange, and user-specified cross-field particle and energy transport coefficients. The equations are discretized on a spatial grid by a finite volume method and solved by fully implicit Newton-Krylov iterations to steady state, which is exact to machine precision. The user must specify the values of the transport coefficients in each cell: the particle diffusivity D, convective velocity

v_{conv}, and electron and ion thermal diffusivities χ_e and χ_i. The cross-field fluxes of particles (Γ_n) and energy (q_e and q_i) are determined by the transport coefficients, the local values of density n, electron and ion temperatures T_e and T_i, and cross-field gradients:

$$\Gamma_n = -D\nabla n + v_{conv} n$$
$$q_{e,i} = -\chi_{e,i} n \nabla T_{e,i} + \frac{5}{2}\Gamma_n T_{e,i}$$

The transport coefficients serve to approximate anomalous transport and are specified by the user such that the model matches a set of target parameters predicted for SPARC, including the heat flux width, power sharing between the inner and outer divertor surfaces, and midplane profiles of density and temperature.

The SPARC SOL is modeled in a double-null equilibrium assuming up-down symmetry for geometry and physics (Figure 2). The radial extent of the domain is $\psi_N \approx 0.98 - 1.04$ in units of standard normalized poloidal magnetic flux, and grid cells are aligned with the flux surfaces. In the simplified model considered here, the target plates are normal to flux surfaces at the strike points, while plates tilted at a shallow angle are planned in the actual SPARC design (a factor of 0.39 on the inboard target and 0.16 on the outer target can be applied to convert from the poloidal heat flux density to the perpendicular heat flux density assuming an incident field line angle of 1º). The grid target surfaces are angled in the far SOL and private flux region in order to alleviate a numerical performance issue with corner cells. The much more open divertor in the UEDGE grid geometry compared to the real SPARC design is a large source of inaccuracy due to neutral baffling effects [9].

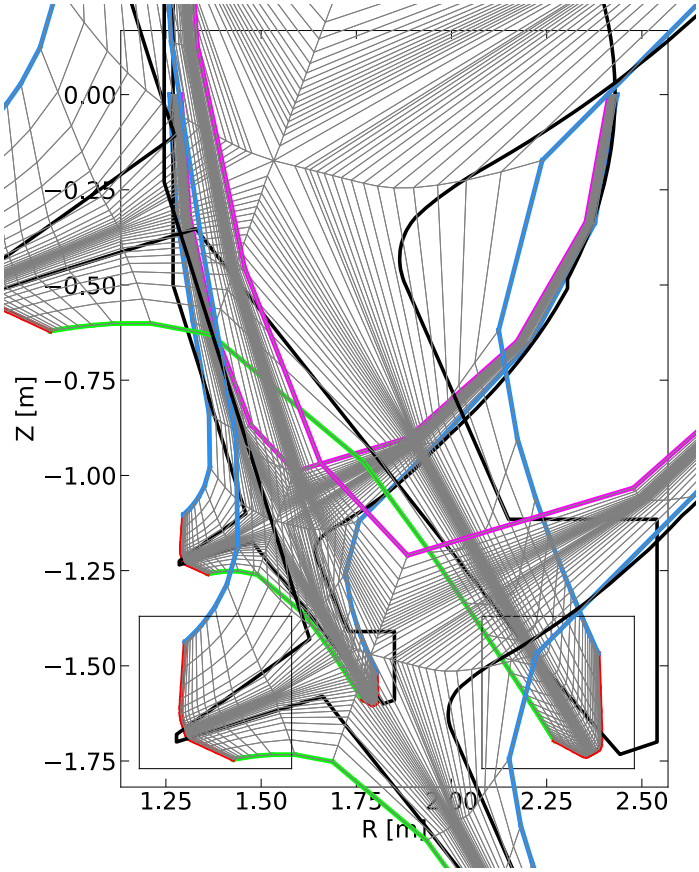

Figure 2: The 2D axisymmetric grid used in this study is shown in gray, and the SPARC first wall geometry is shown in black (the first wall geometry is not included in the simulation). The colored lines are the core boundary (magenta), side wall boundaries (blue), private flux region boundary (green) and target plate boundaries (red).

UEDGE is used in this study to solve for the plasma and neutral densities n_i and n_n (plasma quasineutrality is assumed), electron and ion/neutral temperatures T_e and $T_{i,n}$, and parallel velocities $u_{\parallel i}$ and $u_{\parallel n}$. No single-particle drifts or plasma potential effects are included in this study, due to the up-down symmetry of the setup. The impurity used in this study is carbon, with a concentration specified as a fixed fraction of the main ion density and radiation rates obtained from a non-equilibrium coronal model assuming an impurity lifetime of 1 second (we found the impurity lifetime setting to cause no noticeable change in the UEDGE solutions unless set to a value less than 10 milliseconds). A fluid model is used for the neutral atoms, as the neutral mean free path is expected to be small in the SPARC divertor (in a typical simulation, the neutral charge-exchange mean free path is found in most of the divertor volume to be less than 1 centimeter, which is small compared to the connection length). The fluid neutral model in UEDGE includes inertial effects in the direction parallel to B, to account for strong parallel flows.

The boundary conditions at the core interface are a fixed ion density, zero gradient in parallel velocity, zero neutral flux, and a fixed power divided equally between the ions and electrons. At the target plate boundaries, $v_\parallel = c_s$, and the sheath energy transmission coefficients are $\gamma_e = 4$ and $\gamma_i = 2.5$ (informed by kinetic simulations). Sputtering effects are not included. At the side wall and private flux wall boundaries, the ion density and electron and ion temperature are extrapolated ($\partial^2/\partial r^2 = 0$), with a minimum temperature limit of 0.1 eV. The ion recycling coefficient for all side walls and targets is 1 (appropriate for modeling an experiment in steady state [6]), and the neutral albedo is 1 on all side walls and targets. This means no pumping effects are included in the model. Finally, a heat flux limiter value of 0.21 is used for the electron and ion parallel thermal conduction coefficient. This value is informed by kinetic-fluid modeling [10] and is found to improve agreement between simulation and experiment in Alcator C-Mod [11].

The cross-field transport coefficients in UEDGE were tuned to match several parameters predicted for SPARC using empirical scalings, summarized in Table 1. The transport coefficients satisfying these interrelated constraints were a particle diffusivity of $D = 0.1$ m^2/s and the spatially varying convective velocity v_{conv} and thermal diffusivity $\chi_{e,i}$ shown in Figure 3. These values were tuned using a case with $P_{SOL} = 10$ MW in the full domain and no impurity. The spatial profile of v_{conv} is informed by experiment [12]. The spatial profile of $\chi_{e,i}$ reflects assumptions of reduced energy transport on the high-field side and a transport barrier on the low-field side that strongly affects the outer target heat flux width. The heat flux width in each simulation was measured by fitting a simple exponential curve to the parallel heat flux density at the outer side of the X-point mapped to the outer midplane, and the spreading factor was obtained from an Eich fit [13] to the total surface heat flux at the outer target mapped to the outer midplane. The inner/outer divertor power sharing was calculated by comparing the total power crossing the separatrix on the inboard side to that crossing the separatrix on the outer side.

Table 1: Parameters predicted for SPARC and targeted in UEDGE.

	Expected in SPARC	**Achieved in UEDGE**	**UEDGE controlling variables**
Midplane separatrix density	10^{20} m^{-3} [14]	0.7×10^{20} m^{-3}	D, v_{conv}, n_{core}
Heat flux width λ_q	0.18–0.4 mm [2]	0.23 mm	$D, v_{conv}, \chi_{e,i}$
Heat flux spreading factor S	0.5 λ_q [2]	0.7 λ_q	$D, v_{conv}, \chi_{e,i}$
Inner/outer divertor power sharing	1:4 [3]	1:4	$D, v_{conv}, \chi_{e,i}$

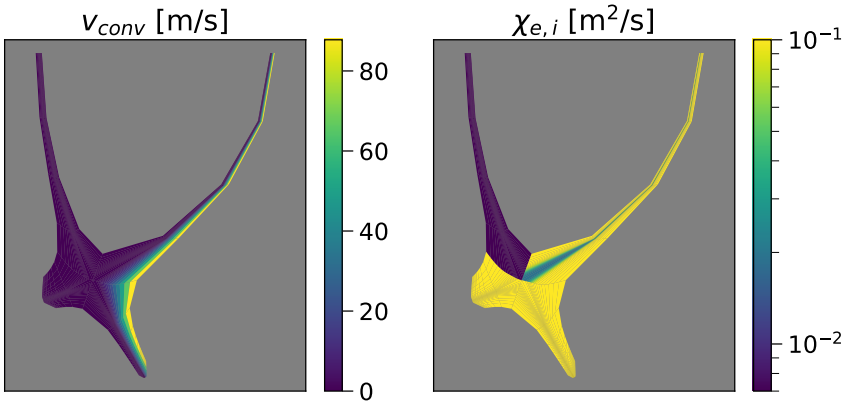

Figure 3: Spatially varying profiles of convective velocity v_{conv} and thermal diffusivity $\chi_{e,i}$ used in this study.

The case with $P_{SOL} = 10$ MW and no impurity, which was used to tune the transport coefficients, has suitable profiles of parallel heat flux density (due to convection and conduction of electrons, ions, and neutrals) at the outer divertor entrance, as well as midplane profiles of T_i, T_e, n_i, and n_n (Figure 4). The portions of the profiles inside the separatrix are not fit to any particular targets and may not be representative of conditions in that region. One interesting feature is the high ion density in the far SOL, where the particle balance is dominated by a radial transport sink and an ionization source at the wall. A flat, high-density "shoulder" is sometimes seen in experiment due to convective radial transport [15], but the high density in the far SOL of these UEDGE simulations appears to be an artifact of the recycling boundary condition that provides a large source of neutrals to be ionized.

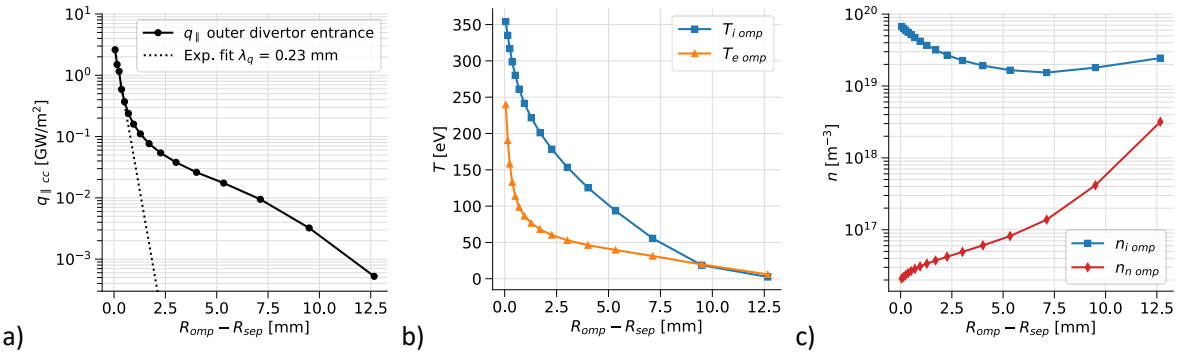

Figure 4: For the case with $P_{SOL} = 10$ MW and 0% carbon fraction, a) the parallel heat flux density due to convected and conducted power at the outer divertor leg entrance (solid line) and a fit to the data with a simple exponential curve (dotted line), b) temperature of the ions (blue) and electrons (orange) at the outer midplane, and c) density of the ions (blue) and neutrals (red) at the outer midplane.

For computational efficiency, the simulations shown in this study are evolved from sequential changes in carbon fraction and input power starting from a single "ancestor" solution rather than each starting from UEDGE's default profiles of density, temperature, and parallel velocity. The "ancestor" solution was started on a crude grid with the transport coefficients set to large values, then changed to the grid and transport coefficients shown in Figure 3. It is important to consider the history of each simulation because solutions can bifurcate [7,16]. The final result of a UEDGE run depends on both the setup parameters and the starting solution. For example, the case with both legs detached at $P_{SOL} = 28$ MW and 1% carbon is obtained starting from the case with only the inner leg detached at $P_{SOL} = 28$ MW and 1% carbon by lowering the power to 16 MW and raising the carbon fraction to 1.4% (at which point both legs are detached) then returning to $P_{SOL} = 28$ MW and 1% carbon while remaining in this new detachment regime.

3. Results

3.1. Scan of P_{SOL} and Carbon Fraction

The SOL input power and carbon fraction were varied in order to characterize a wide range of attached and detached target conditions. One scan began from a solution with the inner target detached and the outer target attached (circles in Figure 5a), while the second scan began from the solution with both targets detached (diamonds in Figure 5a). A large region of overlap can be seen (diamonds superimposed on circles), where both of the bifurcated solutions are possible at identical P_{SOL} and carbon fraction. Both scans were started from $P_{SOL} = 28$ MW and 1% carbon fraction. The power was decreased in steps of 4 MW, and the carbon fraction was raised and lowered in steps of 0.1%. The transition to a fully detached outer leg occurred at $P_{SOL} = 16$ MW when the carbon impurity fraction was raised from 1.3% to 1.4% resulting in a sudden drop in the target temperature, total pressure, heat flux density, and ratio of ion to neutral density. These values remained low over the large range of P_{SOL} and carbon fraction values shown by the diamonds in Figure 5a.

Simulations with lower or higher carbon fraction than those shown in the figure failed to converge. Convergence failures were due to certain cells at the divertor targets reaching negative ion densities because of numerical issues in balancing large fluxes in and out of the cells. These convergence failures arise at low and high carbon fraction, where changes in detachment regime or radiative collapse might be expected, but it is unknown whether the large fluxes at the target cells that cause the numerical issues are physically justified or themselves also due to numerical issues. In light of this uncertainty, this scan can be viewed as a limited window into a simplified model of the detachment regimes possible in SPARC. The upper and lower carbon fraction limits of the scans cannot yet indicate the true operating window of each detachment regime.

Key metrics of detachment are shown in Figure 5b for cases in the scan of power and impurity fraction. The dynamic pressure $m_i n_i v_{\parallel}^2$ at the strike point serves as an indicator of ion momentum removal, which is one aspect of total pressure removal along a field line (due to neutral interactions, radial convection, and viscous dissipation [17]), a key marker of detachment [18]. The ratio of neutral density to ion density characterizes plasma particle loss, and the strike point temperature and peak $q_{\perp}$ can be used to assess energy detachment. The correlations between the parameters in Figure 5b show that momentum removal and energy removal go hand in hand.

Attached and detached target conditions have non-overlapping ranges of target peak $q_{\perp}$ and strike point dynamic pressure but have some overlap in the ranges of strike point n_n/n_i and T_e. The highest values of n_n/n_i around 10^4 are due to very low ion density rather than very high neutral density. The conditions at the inner target (stars in Figure 5b, which are from both sets of cases with the outer leg attached/detached) are similar to those at the detached outer target, indicating that the inner target remains detached throughout the scans. One notable difference between the inner target and detached outer target conditions is in n_n/n_i, which is due to higher average n_i at the inner strike point when the outer leg is detached.

Importantly for the plasma-facing components, the detached targets all have peak $q_{\perp} < 1$ MW/m^2, not including factors for the real geometry with tilted target plates. Of course, the scan also shows that lowering P_{SOL}, for example through increased core radiation, can lower the peak $q_{\perp}$. Finally, the peak heat flux density to the targets can vary significantly in the attached regime for the same P_{SOL}. For example, in the case at full power with the inner leg detached, the peak $q_{\perp}$ at the outer target is 324 MW/m^2 at 0.4% carbon but drops to 39 MW/m^2 at 1.4% carbon, without having fully transitioned to a detached outer leg.

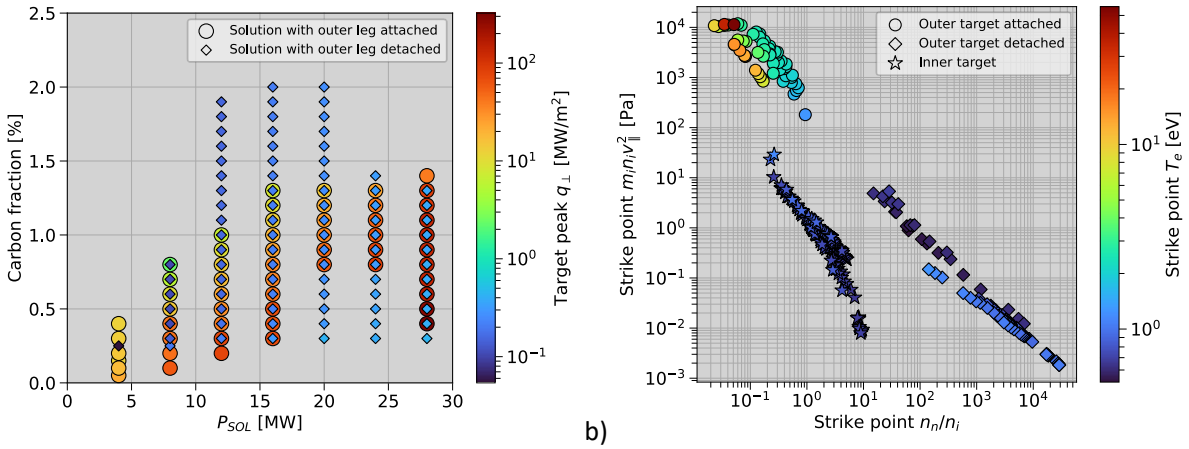

Figure 5: a) Peak total heat flux density perpendicular to the outer target (due to convection, conduction, ion parallel kinetic energy, surface recombination, and radiation) as a function of the SOL input power and carbon fraction. b) Key metrics of detachment measured at the strike points: ratio of neutral to ion density, dynamic pressure, and electron temperature.

3.2. Comparison of Attached and Detached Target Conditions

When the outer leg is attached at full power and 1% carbon fraction, the outer target has a peak $q_\perp \approx 63$ MW/m^2 due to convection and conduction of electrons, ions, and neutrals, $T_{e,i\,max} \approx 4$ eV, $n_{i\,max} \approx 10^{22}$ m^{-3}, and $n_{n\,max} \approx 10^{21}$ m^{-3} (Figure 6). The power delivered to the target due to surface recombination (not shown) is similar in profile and magnitude to the convected and conducted heat flux density, and the power due to impurity radiation reaches a peak of $q_\perp \approx 11$ MW/m^2, as the volume just upstream of the strike-point is highly radiating (Figure 7a). A total of 4.2 MW of power is lost due to impurity radiation in the cells near the X-point, while 5.2 MW is radiated in the volume of the outer leg and only 0.12 MW is radiated in the inner leg. This difference in radiation power loss between the legs is likely due to a difference in temperature: the maximum temperature is 2.5 eV in the volume of the inner leg and 100 eV in the volume of the outer leg, and the peak in the radiated power cooling rate coefficient for carbon is about 10 eV [19].

The solution with a detached outer leg at full power and 1% carbon fraction shows a peak $q_\perp \approx 2.5$ kW/m^2 due to convection and conduction, $T_{e,i\,max} \approx 2.5$ eV, $n_{i\,max} \approx 10^{18}$ m^{-3}, and $n_{n\,max} \approx 2 \times 10^{20}$ m^{-3} (Figure 6). In this scenario, impurity radiation produces a peak of only $q_\perp \approx 0.32$ MW/m^2 at the outer target, as 9.9 MW of power is lost due to radiation near the X-point and only negligible amounts are lost in the volume of either leg (Figure 7b). Core performance is unaffected, however, as only 0.12 MW of power is lost to radiation inside the separatrix. In both cases with and without detachment of the outer leg, the total power lost due to deuterium radiation is 1–1.4 MW from ionization and 1.4–1.6 MW from recombination.

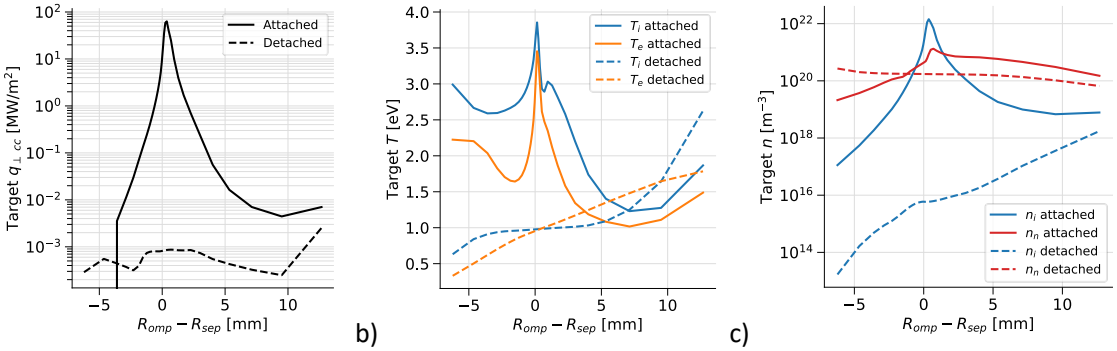

Figure 6: Comparison of plasma parameters at the outer target mapped to the outer midplane for the attached case (solid lines) and detached case (dashed lines) at $P_{SOL} = 28$ MW and 1% carbon fraction, showing a) the convected and conducted heat flux density perpendicular to the target, b) the temperature of the ions (blue) and electrons (orange), and c) the density of the ions (blue) and neutrals (red).

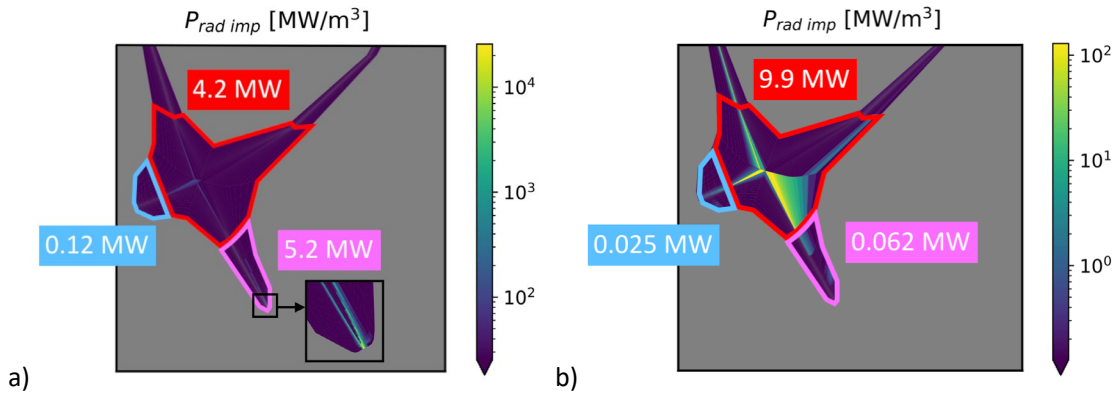

Figure 7: Carbon impurity radiation at $P_{SOL} = 28$ MW and 1% carbon fraction in a) the case with the inner leg detached and outer leg attached and b) the case with both legs detached. The total power loss due to impurity radiation is indicated in red for cells adjacent to the X-point, blue for cells in the inner divertor leg, and magenta for cells in the outer divertor leg.

3.3. Sensitivity to Boundary Conditions

In order to determine the sensitivity of the solutions to various aspects of the simulation setup, certain assumptions were varied to note the effect on the convected and conducted heat flux at the outer target (Figure 8a). The original case, with an attached outer leg, had extrapolated values of temperature in the range of 0.1 eV < T_i < 4 eV for the common flux region radial boundary and 1 eV < T_i < 5 eV for the private flux region boundary. When the extrapolation boundary conditions were all changed to gradient-length type with an infinite gradient length, the outer leg became fully detached. This result held for gradient lengths as low as 1 centimeter. Changing from the extrapolation boundary condition to a fixed value similarly upended the original result. Setting a fixed boundary value of 2 eV for the ion temperature on the radial boundary of the common flux region caused a large increase in heat flux to the outer leg, while doing so instead on the private flux region boundary had the opposite effect, causing the outer leg to completely detach. For the private flux boundary, a threshold was observed: the outer leg would detach if the boundary temperature was fixed to less than 2.3 eV and would remain attached if the boundary temperature was fixed to a higher value (while still having a noticeable effect on the peak heat flux density). This sensitivity to different values of the fixed boundary condition shows the utility of the extrapolation boundary conditions in allowing the absolute value and gradient to float.

The outer strike plate geometry was also found to have a large impact on the overall solution (Figure 8a,b) at $P_{SOL} = 28$ MW and 1% carbon fraction. A grid was produced in which the outer divertor strike plate was tilted to more closely match the as-designed SPARC divertor surfaces. The new target geometry still does not match the SPARC design perfectly due to grid generator issues encountered when attempting to further increase fidelity. There are also fundamental limitations in UEDGE which make it impossible to include the shadowed corner volume in the bottom right. The new grid target plate has a slightly less grazing angle than the SPARC design, with slopes differing by 5.5º in the poloidal plane. The incident field line angle at the separatrix is 1.66º in the new grid (compared to 6.36º in the grid shown in Figure 2 used in the rest of this study), which is close to the target value of 1º and less than the 2º upper limit considered in the SPARC design [2]. In the simulation with the new grid, a factor of 3.9 reduction in the peak heat flux at the outer target was expected due to the increase in surface area at the strike plate near the separatrix, but a much larger degree of power detachment is instead observed: the peak heat flux is three orders of magnitude smaller than in the case where the plate was not tilted. At the outer target separatrix, the electron temperature is 1.2 eV, and the ratio of neutral to ion density is 4.8. These values are similar to those of the detached inner target, but the ratio of neutral to ion density is lower than that at the outer target in cases where the outer leg is fully detached (Figure 5). In light of these results, the grid without tilted target plates that was used throughout this work can be seen as overestimating the carbon fraction required to detach (not to imply that the present setup had any strong ability to predict absolute detachment thresholds in

experiment), although this statement is weakened by unresolved differences in baffling between the real SPARC geometry and the grid with tilted targets.

In all cases where the boundary conditions were changed or the target plate was tilted, the heat flux width measured at the outer divertor entrance remained in the range of 0.2–0.3 millimeters. While the degree of detachment changes significantly with the boundary conditions, it is reassuring that the heat flux width does not.

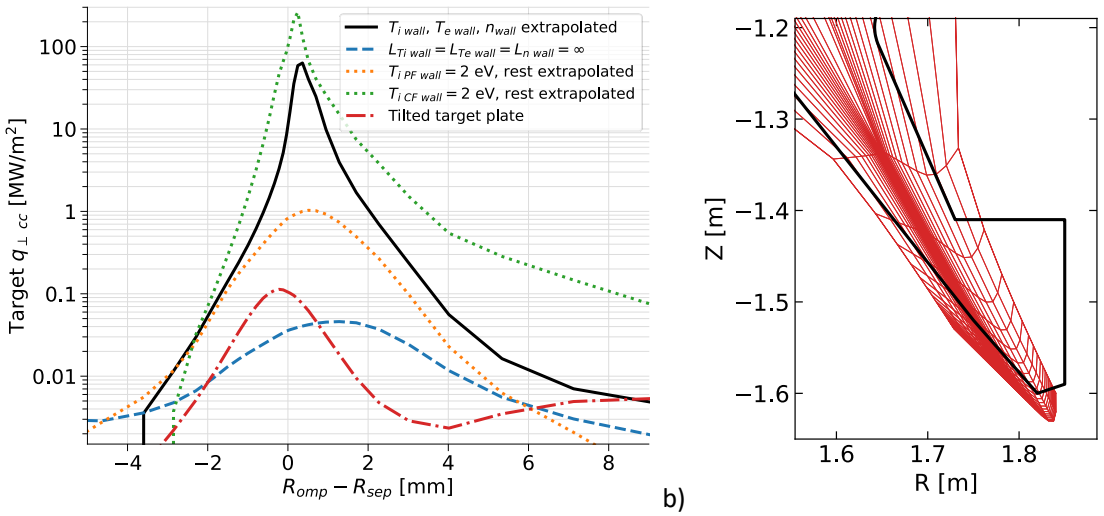

Figure 8: a) Heat flux density due to convection and conduction perpendicular to the outer target mapped to the outer midplane. The original case with $P_{SOL} = 28$ MW and 1% carbon fraction is shown in black and has extrapolated density and temperature values on the radial boundaries. The dashed blue line shows the result of setting all radial boundary values based on an infinite gradient length ($L_T = T/\nabla T = \infty$). The dotted orange line shows the result of changing the ion temperature boundary condition on the private flux region radial boundary to be fixed at 2 eV rather than extrapolated. The dotted green line shows the result of fixing the ion temperature to 2 eV on the common flux region radial boundary. The red dash-dotted line shows the result of changing the outer target plate geometry to that shown in subfigure b). b) (Red) UEDGE mesh with an outer target geometry better matching the tilt of the as-designed SPARC divertor geometry (black).

3.4. Sensitivity to the Neutral Fraction

In addition to the carbon fraction, the neutral fraction is an important factor in simulation results. The neutral fraction is defined here as the total number of neutrals in the full domain divided by the total number of ions. A case at $P_{SOL} = 10$ MW and 0% carbon with both legs attached has a ~5% neutral fraction. At $P_{SOL} = 28$ MW and 1% carbon fraction, the case with only the inner leg detached has a neutral fraction of ~10%, and the case with both legs detached has a neutral fraction of ~20%. In order to determine whether neutral sources or sinks would have a significant effect on the $P_{SOL} = 28$ MW cases, a neutral pumping/puffing surface was defined on the outer leg common flux region boundary, with user-specified neutral throughput. The neutral pumping or puffing rate can change the neutral fraction by a few percent before solutions begin to have trouble converging (Figure 9a). Raising the neutral fraction results in a lower peak convected and conducted heat flux density on the outer target (Figure 9b). This trend holds when both legs are detached and when only the inner leg is detached. For the case with only the inner leg detached, the fact that the highest pumping rate results in a neutral fraction around 5% might lead one to expect that the inner leg would reattach, however it remains detached. The neutral fraction therefore does not perfectly determine each detachment regime, but it may partially explain why different solutions are possible at the same P_{SOL} and carbon fraction.

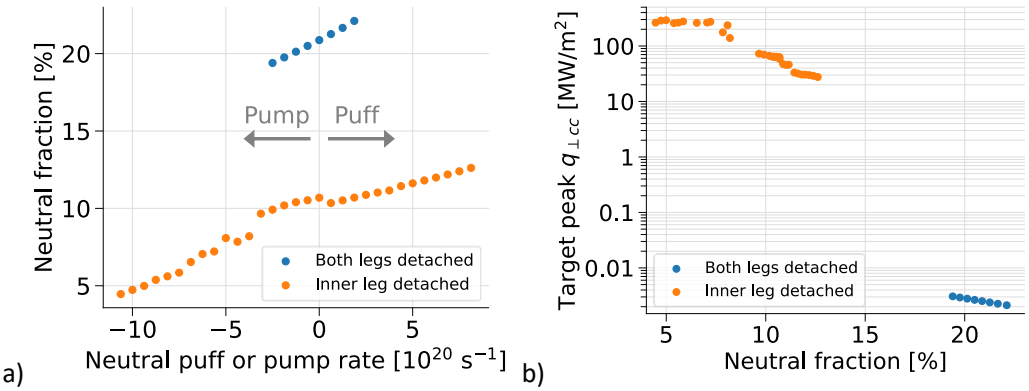

Figure 9: All cases have $P_{SOL} = 28$ MW and 1% carbon fraction. a) The total neutral fraction as a function of the neutral puff or pump rate in the outer leg. b) Peak heat flux density due to convection and conduction to the outer divertor target as a function of the total neutral fraction.

3.5. Comparison to SOLPS

SOLPS-ITER [20] simulations of SPARC [21] have been developed alongside UEDGE ones in a parallel, independent effort. The SOLPS simulations use more sophisticated neutral and impurity models and a more realistic geometry, while the UEDGE cases are simpler in most respects. The UEDGE setup has been convenient for large parameter scans like the ones in this study, and the more accurate SOLPS cases can be useful to roughly check the validity of certain simplifying assumptions in UEDGE. Due to the large differences in setup between the codes, this comparison cannot serve as a validation exercise. Table 2 summarizes the differences in setup between a UEDGE case with no pumping and the most comparable SOLPS case (found by lowering the pumping rate in the SOL volume in SOLPS). The cases have similar peak $q_{\parallel}$ and have peak densities at the outer target within a factor of 3.

Table 2: Comparison of UEDGE and SOLPS simulations of SPARC at $P_{SOL} = 28$ MW.

	UEDGE	**SOLPS**
Magnetic configuration	Double null	Single null
Target plates	Not tilted	Tilted
Simulation domain	Near SOL	Near SOL (+far SOL for neutrals)
Neutral model	Fluid neutrals	Kinetic neutrals
Impurity model	Fixed fraction	Transported impurities
Pumping	No	Yes
Carbon chemical sputtering	0%	2%
Carbon fraction	1%	1.7%
Outer target peak $q_{\parallel}$ [GW/m^2]	0.57	0.42
Outer target peak n_i [m^{-3}]	1.4×10^{22}	0.57×10^{22}

The fixed carbon fraction used in UEDGE can be compared to the spatial distribution of carbon resulting from the transported impurity model with multiple charge states in the SOLPS case. In the UEDGE case, the carbon density is defined everywhere as 1% of the ion density. In the SOLPS case, the carbon released from sputtering and transported in the model results in a carbon fraction as low as 0.3% and as high as 40% in a small number of cells, with more typical values in the SOL in the range of 1–4%, resulting in an average of 1.7% over the entire domain. The charge states of carbon that reach the highest densities in the divertor legs are C^+ and C^{2+}, reaching peaks of 10^{20} m^{-3} while other charge states have peak densities of 10^{19} m^{-3} or lower. While the discrepancy in carbon fraction between SOLPS is on the order of a few percent in most of the cells, highly radiating cells near the targets can account for a large fraction of the power

dissipated through impurity radiation (see Figure 7a). The SOLPS impurity transport model therefore offers much more detail than the fixed impurity fraction model and could have a large impact on the UEDGE solutions. An impurity transport model is available in UEDGE but has so far caused convergence difficulties when enabled.

The UEDGE case uses a fluid neutral model with inertia but assumes that the neutral temperature is equal to the ion temperature everywhere. In reality, the neutral temperature could be much lower than the ion temperature near the walls before the two equilibrate through charge exchange collisions. In the SOLPS case, the kinetic neutral model provides some indication of the variation in neutral temperature to be expected. The ratio of neutral to ion temperature ranges between 0.5–1 in most of the domain, with values close to 2 occurring in the divertor regions where the plasma temperature is low. The charge exchange and ionization mean free paths for deuterium atoms near the Franck-Condon energy in the SOLPS case are less than 1 centimeter in most of the domain except the very far SOL where they can be greater than 1 meter. These neutral temperature and mean free path results from SOLPS indicate that the UEDGE fluid neutral model is not an egregious simplification.

Like the UEDGE case, the SOLPS case is also sensitive to neutral pumping rates, especially when the pumping rate in the outer divertor is varied. This has a large impact on $q_{\parallel}$ and the average carbon fraction: in the original SOLPS case, the average carbon fraction was 5% and the peak $q_{\parallel}$ was around 4 GW/m^2, which changed to 1.7% and 0.57 GW/m^2 as the pumping rate in the outer divertor was decreased. The average carbon fraction in SOLPS is more a function of the overall plasma and neutral density (which affect the carbon sputtering source) than a function of the carbon being directly pumped out. In any case, the sensitivity of both UEDGE and SOLPS to the neutral pumping rate underscore the importance of this quantity for either code to have predictive power.

4. Conclusions

UEDGE simulations yielding detached divertor target conditions in a SPARC double-null equilibrium with $P_{SOL} = 28$ MW show markedly low target temperatures, ion densities, and heat fluxes. This result shows that planned "full-power" SPARC operation could be compatible with plasma-facing components (PFCs) even without strike-point sweeping. Peak heat flux densities from detached plasmas are typically around $q_{\perp} \approx 0.8$ MW/m^2, dominated by impurity radiation. Cases with the inner leg or both legs detached are obtained with a carbon fraction between 0.3–1.4%. This study cannot predict a definitive value of the carbon fraction required to detach due to the large simplifications in the model and convergence difficulties at high and low carbon fraction.

The small carbon fraction at which detachment may be possible could have advantages and disadvantages. The detrimental effect of around 1% carbon on core performance due to increased Z_{eff} is small: a 1% carbon fraction, fully ionized, results in $Z_{\mathrm{eff}} = 1.3$, and TRANSP simulations predict that SPARC should be able to maintain $Q > 2$ up to $Z_{\mathrm{eff}} = 3.4$ [22]. The stability and control of detachment, however, are of some concern, as it may be difficult to *avoid* detachment if graphite is chosen as a divertor material and enough carbon is released through sputtering. Furthermore, in the regime where both legs are detached, the radiation pattern concentrated near the X-point is similar to an X-point MARFE, which can terminate the discharge [23]. Stable operation in this regime is not impossible, however, as demonstrated by experiments on the AUG tokamak with a tungsten wall and neon impurity seeding [24].

The results of this study indicate that detachment through impurity seeding in SPARC may provide significant benefits in the divertor heat flux handling challenge. Future work is planned to refine these results by modeling realistic tilted target plates and neutral baffles, using a multi-fluid impurity model rather than the fixed-fraction model, seeding with other impurities such as neon (which would likely be used if a tungsten-based material is chosen for the plasma-facing components), and modeling electric fields, drifts, and currents. These results will serve as starting points and points of comparison for additional UEDGE simulations of the single-null and X-point target [25] configurations that are also planned for SPARC.

Acknowledgements

This work was supported by

- The INFUSE program: a DOE SC FES private private-public partnership program, grant TC02335
- Commonwealth Fusion Systems RPP007
- The SPARC Fellowship Fund
- The Samuel W. Ing (1953) Memorial Fund, a gift of Mimi and Frank Slaughter

Bibliography

[1] A.J. Creely, M.J. Greenwald, S.B. Ballinger, D. Brunner, J. Canik, J. Doody, T. Fülöp, D.T. Garnier, R. Granetz, T.K. Gray, C. Holland, N.T. Howard, J.W. Hughes, J.H. Irby, V.A. Izzo, G.J. Kramer, A.Q. Kuang, B. Labombard, Y. Lin, B. Lipschultz, N.C. Logan, J.D. Lore, E.S. Marmar, K. Montes, R.T. Mumgaard, C. Paz-Soldan, C. Rea, M.L. Reinke, P. Rodriguez-Fernandez, K. Särkimäki, F. Sciortino, S.D. Scott, A. Snicker, P.B. Snyder, B.N. Sorbom, R. Sweeney, R.A. Tinguely, E.A. Tolman, M. Umansky, O. Vallhagen, J. Varje, D.G. Whyte, J.C. Wright, S.J. Wukitch, J. Zhu, Overview of the SPARC tokamak, J. Plasma Phys. (2020). https://doi.org/10.1017/S0022377820001257.

[2] A.Q. Kuang, S. Ballinger, D. Brunner, J. Canik, A.J. Creely, T. Gray, M. Greenwald, J.W. Hughes, J. Irby, B. Labombard, B. Lipschultz, J.D. Lore, M.L. Reinke, J.L. Terry, M. Umansky, D.G. Whyte, S. Wukitch, Divertor heat flux challenge and mitigation in SPARC, J. Plasma Phys. (2020). https://doi.org/10.1017/S0022377820001117.

[3] D. Brunner, A.Q. Kuang, B. Labombard, J.L. Terry, The dependence of divertor power sharing on magnetic flux balance in near double-null configurations on Alcator C-Mod, Nucl. Fusion. 58 (2018). https://doi.org/10.1088/1741-4326/aac006.

[4] M.L. Reinke, Heat flux mitigation by impurity seeding in high-field tokamaks, Nucl. Fusion. 57 (2017). https://doi.org/10.1088/1741-4326/aa5145.

[5] T.D. Rognlien, J.L. Milovich, M.E. Rensink, G.D. Porter, A fully implicit, time dependent 2-D fluid code for modeling tokamak edge plasmas, J. Nucl. Mater. 196–198 (1992) 347–351. https://doi.org/10.1016/S0022-3115(06)80058-9.

[6] M. V Umansky, M.E. Rensink, T.D. Rognlien, B. LaBombard, D. Brunner, J.L. Terry, D.G. Whyte, Assessment of X-point target divertor configuration for power handling and detachment front control, Nucl. Mater. Energy. (2017) 1–6. https://doi.org/10.1016/j.nme.2017.03.015.

[7] M.R.K. Wigram, B. Labombard, M. V. Umansky, A.Q. Kuang, T. Golfinopoulos, J.L. Terry, D. Brunner, M.E. Rensink, C.P. Ridgers, D.G. Whyte, Performance assessment of long-legged tightly-baffled divertor geometries in the ARC reactor concept, Nucl. Fusion. 59 (2019). https://doi.org/10.1088/1741-4326/ab394f.

[8] D. Brunner, B. Labombard, A.Q. Kuang, J.L. Terry, High-resolution heat flux width measurements at reactor-level magnetic fields and observation of a unified width scaling across confinement regimes in the Alcator C-Mod tokamak, Nucl. Fusion. 58 (2018). https://doi.org/10.1088/1741-4326/aad0d6.

[9] A. Loarte, Effects of divertor geometry on tokamak plasmas, Plasma Phys. Control. Fusion. 43 (2001) R183–R224. https://doi.org/10.1088/0741-3335/43/6/201.

[10] Z. Abou-Assaleh, J.P. Matte, T.W. Johnston, R. Marchand, Fokker-Planck Modelling of Edge Plasma Near the Neutralizer Plate in a Tokamak, Contrib. to Plasma Phys. 32 (1992) 268–272. https://doi.org/10.1002/ctpp.2150320315.

[11] D. Brunner, B. Labombard, R.M. Churchill, J. Hughes, B. Lipschultz, R. Ochoukov, T.D. Rognlien, C. Theiler, J. Walk, M. V. Umansky, D. Whyte, An assessment of ion temperature measurements in the boundary of the Alcator C-Mod tokamak and implications for ion fluid heat flux limiters, Plasma Phys. Control. Fusion. 55 (2013). https://doi.org/10.1088/0741-3335/55/9/095010.

[12] B. Lipschultz, D. Whyte, B. LaBombard, Comparison of particle transport in the scrape-off layer plasmas of Alcator C-Mod and DIII-D, Plasma Phys. Control. Fusion. 47 (2005) 1559–1578. https://doi.org/10.1088/0741-3335/47/10/001.

[13] T. Eich, A.W. Leonard, R.A. Pitts, W. Fundamenski, R.J. Goldston, T.K. Gray, A. Herrmann, A. Kirk, A. Kallenbach, O. Kardaun, A.S. Kukushkin, B. Labombard, R. Maingi, M.A. Makowski, A. Scarabosio, B. Sieglin,

J. Terry, A. Thornton, Scaling of the tokamak near the scrape-off layer H-mode power width and implications for ITER, Nucl. Fusion. 53 (2013). https://doi.org/10.1088/0029-5515/53/9/093031.
[14] A.S. Kukushkin, G. Janeschitz, A. Loarte, H.D. Pacher, D. Coster, D. Reiter, R. Schneider, Critical issues in divertor optimisation for ITER-FEAT, J. Nucl. Mater. 290–293 (2001) 887–891. https://doi.org/10.1016/S0022-3115(00)00457-8.
[15] B. LaBombard, J.W. Hughes, D. Mossessian, M. Greenwald, B. Lipschultz, J.L. Terry, Evidence for electromagnetic fluid drift turbulence controlling the edge plasma state in the Alcator C-Mod tokamak, Nucl. Fusion. 45 (2005) 1658–1675. https://doi.org/10.1088/0029-5515/45/12/022.
[16] F. Wising, D.A. Knoll, S.I. Krasheninnikov, T.D. Rognlien, D.J. Sigmar, Simulation of Detachment in ITER-Geometry Using the UEDGE Code and a Fluid Neutral Model, Contrib. to Plasma Phys. 36 (1996) 309–313. https://doi.org/10.1002/ctpp.2150360238.
[17] M. V. Umansky, D. Brunner, B. Labombard, T.D. Rognlien, Modeling of Local Edge Plasma Perturbations Induced by a Biased Probe, Contrib. to Plasma Phys. 52 (2012) 417–423. https://doi.org/10.1002/ctpp.201210026.
[18] Stangeby, The Plasma Boundary of Magnetic Fusion Devices, Institute of Physics Publishing, Bristol, 2000. https://www.taylorfrancis.com/books/9781420033328.
[19] P.G. Carolan, V.A. Piotrowicz, The behaviour of impurities out of coronal equilibrium, Plasma Phys. 25 (1983) 1065–1086. https://doi.org/10.1088/0032-1028/25/10/001.
[20] S. Wiesen, D. Reiter, V. Kotov, M. Baelmans, W. Dekeyser, A.S. Kukushkin, S.W. Lisgo, R.A. Pitts, V. Rozhansky, G. Saibene, I. Veselova, S. Voskoboynikov, The new SOLPS-ITER code package, J. Nucl. Mater. 463 (2015) 480–484. https://doi.org/10.1016/j.jnucmat.2014.10.012.
[21] J. Lore, J.M. Canik, A.Q. Kuang, B. LaBombard, B. Lipschultz, M.L. Reinke, Predictive modeling of SPARC divertor conditions using SOLPS-ITER, Bull. Am. Phys. Soc. (2020). https://meetings.aps.org/Meeting/DPP20/Session/BP13.4.
[22] P. Rodriguez-Fernandez, N.T. Howard, M.J. Greenwald, A.J. Creely, J.W. Hughes, J.C. Wright, C. Holland, Y. Lin, F. Sciortino, Predictions of core plasma performance for the SPARC tokamak, J. Plasma Phys. (2020) 1–24. https://doi.org/10.1017/S0022377820001075.
[23] B. Lipschultz, J.L. Terry, C. Boswell, J.A. Goetz, A.E. Hubbard, S.I. Krasheninnikov, B. LaBombard, D.A. Pappas, C.S. Pitcher, F. Wising, S. Wukitch, The role of particle sinks and sources in Alcator C-Mod detached divertor discharges, Phys. Plasmas. 6 (1999) 1907–1916. https://doi.org/10.1063/1.873448.
[24] F. Reimold, M. Wischmeier, M. Bernert, S. Potzel, A. Kallenbach, H.W. Müller, B. Sieglin, U. Stroth, Divertor studies in nitrogen induced completely detached H-modes in full tungsten ASDEX Upgrade, Nucl. Fusion. 55 (2015). https://doi.org/10.1088/0029-5515/55/3/033004.
[25] B. LaBombard, E. Marmar, J. Irby, J.L. Terry, R. Vieira, G. Wallace, D.G. Whyte, S. Wolfe, S. Wukitch, S. Baek, W. Beck, P. Bonoli, D. Brunner, J. Doody, R. Ellis, D. Ernst, C. Fiore, J.P. Freidberg, T. Golfinopoulos, R. Granetz, M. Greenwald, Z.S. Hartwig, A. Hubbard, J.W. Hughes, I.H. Hutchinson, C. Kessel, M. Kotschenreuther, R. Leccacorvi, Y. Lin, B. Lipschultz, S. Mahajan, J. Minervini, R. Mumgaard, R. Nygren, R. Parker, F. Poli, M. Porkolab, M.L. Reinke, J. Rice, T. Rognlien, W. Rowan, S. Shiraiwa, D. Terry, C. Theiler, P. Titus, M. Umansky, P. Valanju, J. Walk, A. White, J.R. Wilson, G. Wright, S.J. Zweben, ADX: A high field, high power density, advanced divertor and RF tokamak, Nucl. Fusion. 55 (2015). https://doi.org/10.1088/0029-5515/55/5/053020.